Monthly Notices
of the
ROYAL ASTRONOMICAL SOCIETY

Mon. Not. R. Astron. Soc. **414,** 1903–1913 (2011) doi:10.1111/j.1365-2966.2011.18499.x

Infrared luminosity functions of *AKARI* Sloan Digital Sky Survey galaxies

Tomotsugu Goto,[1,2]★ Stephane Arnouts,[3] Matthew Malkan,[4] Toshinobu Takagi,[5] Hanae Inami,[6] Chris Pearson,[7,8,9] Takehiko Wada,[5] Hideo Matsuhara,[5] Chisato Yamauchi,[5] Tsutomu T. Takeuchi,[10,11] Takao Nakagawa,[5] Shinki Oyabu,[11] Daisuke Ishihara,[11] David B. Sanders,[1] Emeric Le Floc'h,[12] Hyung Mok Lee,[13] Woong-Seob Jeong,[14] Stephen Serjeant[9] and Chris Sedgwick[9]

[1]*Institute for Astronomy, University of Hawaii, 2680 Woodlawn Drive, Honolulu, HI 96822, USA*
[2]*Subaru Telescope 650 North A'ohoku Place Hilo, HI 96720, USA*
[3]*Canada–France–Hawaii Telescope, 65-1238 Mamalahoa Hwy, Kamuela, Hawaii 96743, USA*
[4]*Department of Physics and Astronomy, UCLA, Los Angeles, CA 90095-1547, USA*
[5]*Institute of Space and Astronautical Science, Japan Aerospace Exploration Agency, Sagamihara, Kanagawa 252-5210, Japan*
[6]*Spitzer Science Center, California Institute of Technology, Pasadena, CA 91125, USA*
[7]*RAL Space, Rutherford Appleton Laboratory, Chilton, Didcot, Oxfordshire OX11 0QX*
[8]*Institute for Space Imaging Science, University of Lethbridge, Lethbridge, Alberta T1K 3M4, Canada*
[9]*Astrophysics Group, Department of Physics, The Open University, Milton Keynes MK7 6AA*
[10]*Institute for Advanced Research, Nagoya University, Furo-cho, Chikusa-ku, Nagoya 464-8601, Japan*
[11]*Division of Particle and Astrophysical Science, Nagoya University, Furo-cho, Chikusa-ku, Nagoya 464-8602, Japan*
[12]*CEA-Saclay, Service d'Astrophysique, France*
[13]*Department of Physics & Astronomy, FPRD, Seoul National University, Shillim-Dong, Kwanak-Gu, Seoul 151-742, Korea*
[14]*Korea Astronomy and Space Science Institute 61-1, Hwaam-dong, Yuseong-gu, Daejeon 305-348, Republic of Korea*

Accepted 2011 February 8. Received 2011 January 19; in original form 2010 September 23

ABSTRACT

By cross-correlating the *AKARI* all-sky survey in six infrared (IR) bands (9, 18, 65, 90, 140 and 160 μm) with the Sloan Digital Sky Survey (SDSS) galaxies, we identified 2357 IR galaxies with a spectroscopic redshift. This is not just one of the largest samples of local IR galaxies, but *AKARI* provides crucial far-IR (FIR) bands for accurately measuring the galaxy spectral energy distribution (SED) across the peak of the dust emission at >100 μm. By fitting modern IR SED models to the *AKARI* photometry, we measured the total infrared luminosity ($L_{\rm IR}$) of individual galaxies.

Using this $L_{\rm IR}$, we constructed the luminosity functions (LF) of IR galaxies at a median redshift of $z = 0.031$. The LF agrees well with that at $z = 0.0082$ (the Revised Bright Galaxy Sample), showing smooth and continuous evolution towards higher redshift LFs measured in the *AKARI* North Ecliptic Pole (NEP) deep field. By integrating the IR LF weighted by $L_{\rm IR}$, we measured the local cosmic IR luminosity density of $\Omega_{\rm IR} = (3.8^{+5.8}_{-1.2}) \times 10^8\,{\rm L}_\odot\,{\rm Mpc}^{-3}$. We separate galaxies into active galactic nuclei (AGN), star-forming galaxies (SFG) and composite by using the [N II]/Hα versus [O III]/Hβ line ratios. The fraction of AGN shows a continuous increase with increasing $L_{\rm IR}$ from 25 to 90 per cent at $9 < \log L_{\rm IR} < 12.5$. The ${\rm SFR}_{\rm H\alpha}$ and $L_{\rm [O\,III]}$ show good correlations with $L_{\rm IR}$ for SFG and AGN, respectively. The self-absorption-corrected Hα/Hβ ratio shows a weak increase with $L_{\rm IR}$ with a substantial scatter. When we separate IR LFs into contributions from AGN and SFG, the AGN contribution becomes dominant at $L_{\rm IR} > 10^{11}\,{\rm L}_\odot$, coinciding with the break of both the SFG and AGN IR LFs. At $L_{\rm IR} \leq 10^{11}\,{\rm L}_\odot$, SFG dominates IR LFs. Only 1.1 ± 0.1 per cent of $\Omega_{\rm IR}$ is produced by luminous infrared galaxies ($L_{\rm IR} > 10^{11}\,{\rm L}_\odot$), and only 0.03 ± 0.01 per cent by ultraluminous infrared galaxies ($L_{\rm IR} > 10^{12}\,{\rm L}_\odot$) in the local Universe. Compared with high-redshift results

★E-mail: tomo@ifa.hawaii.edu

from the *AKARI* NEP deep survey, we observed a strong evolution of $\Omega_{\rm IR}^{\rm SFG} \propto (1+z)^{4.1\pm0.4}$ and $\Omega_{\rm IR}^{\rm AGN} \propto (1+z)^{4.1\pm0.5}$. Our results show that all of our measured quantities (IR LFs, L^*, $\Omega_{\rm IR}^{\rm AGN}$, $\Omega_{\rm IR}^{\rm SFG}$) show smooth and steady increase from lower redshift (the Revised Bright Galaxy Sample) to higher redshift (the *AKARI* NEP deep survey).

Key words: galaxies: evolution – galaxies: formation – galaxies: interactions – galaxies: peculiar – galaxies: starburst – infrared: galaxies.

1 INTRODUCTION

To understand the cosmic history of star formation (SF) and active galactic nuclei (AGN), it is vital to understand infrared (IR) emission; the more intense the SF is, the more deeply it is embedded in the dust, hence such SF is not visible in the ultraviolet (UV) but in the IR. Similarly, AGN evolutionary scenarios predict that AGN are heavily obscured at their youngest, Compton-thick stage (Treister, Urry & Virani 2009). The *Spitzer* and *AKARI* satellites revealed a great deal of IR emission in the high-redshift Universe, showing strong evolution in the IR luminosity density (Le Floc'h et al. 2005; Pérez-González et al. 2005; Babbedge et al. 2006; Caputi et al. 2007; Magnelli et al. 2009; Goto et al. 2010b; Gruppioni et al. 2010; Rodighiero et al. 2010). For example, at $z = 1$, Goto et al. (2010a) estimated 90 per cent of SF activity is hidden by dust.

However, to investigate the evolution of the IR luminosity function (LF), these high-redshift studies need a good comparison sample at $z = 0$. Even today, the often used one is the *IRAS* LFs (Rush, Malkan & Spinoglio 1993; Sanders et al. 2003; Goto et al. 2011) from the 1980s, with only several hundred galaxies. In addition, for more than 25 years, bolometric IR luminosities ($L_{\rm IR,8-1000\,\mu m}$) of local galaxies have been estimated using an equation in Pérault (1987), which is a simple polynomial, obtained assuming a simple blackbody and dust emissivity. Furthermore, the reddest filter of *IRAS* is 100 μm, which does not span the peak of the dust emission for most galaxies, leaving a great deal of uncertainty. A number of studies found cold dust that cannot be detected with *IRAS*. For example, Dunne & Eales (2001) detected such cold dust with $T \sim 20$ K using SCUBA 450 and 850 μm fluxes. Symeonidis et al. (2009) detected cold galaxies with SED peaks at longer wavelengths using *Spitzer*. These results cast further doubt on $L_{\rm IR}$ estimated using only $<$100 μm photometry. A more precise estimate of the local $L_{\rm IR}$ and thus the local IR LF has been long awaited, to be better compared with high-redshift work and to understand where the end-point of the cosmic IR density evolution is.

AKARI, the Japanese IR satellite (Murakami et al. 2007), provides the first chance to rectify the situation since *IRAS*; *AKARI* performed an all-sky survey in two mid-IR bands (centred on 9 and 18 μm) and in four far-IR (FIR) bands (65, 90, 140 and 160 μm). Its 140 and 160 μm sensitivities are especially important to cover across the peak of the dust emission, allowing us to accurately measure the Rayleigh–Jeans tail of the IR emission.

Using deeper data and modern models, in this work, we aim to measure local $L_{\rm IR}$, and thereby the IR LF. By matching the *AKARI* IR sources with the Sloan Digital Sky Survey (SDSS) galaxies, our sample contains ∼2357 IR galaxies. Compared to previous work (Sanders et al. 2003; Goto et al. 2011), the sample is several times larger, allowing us to accurately measure the IR LF of the local Universe. The optical spectra of the SDSS also allow us to separate IR emission from AGN and star-forming galaxies (SFG). This work provides us with an important local benchmark to base our evolution studies at high redshift both by the current *AKARI*, *Spitzer* and *Herschel* satellites, and by next-generation IR satellites such as the *Wide-Field Infrared Survey Explorer (WISE)*, the *James Webb Space Telescope (JWST)* and the *Space Intra-red Telescope for Cosmology and Astrophysics (SPICA)*. Following Sanders et al. (2003), we adopt a cosmology with $(h, \Omega_{\rm m}, \Omega_\Lambda) = (0.75, 0.3, 0.7)$.

2 DATA AND ANALYSIS

2.1 *AKARI*-SDSS sample

AKARI (Murakami et al. 2007) performed an all-sky survey in two mid-IR bands (centred on 9 and 18 μm) and in four FIR bands (65, 90, 140 and 160 μm). In this work, we use version 1 of the *AKARI*/Infrared Camera (IRC) point source catalogue and the *AKARI*/FIS bright source catalogue, which is selected at 90 μm. The 5σ sensitivities in the *AKARI* IR filters (*S*9*W*, *L*18*W*, *N*60, *WS*, *WL* and *N*160) are 0.05, 0.09, 2.4, 0.55, 1.4 and 6.3 Jy (Yamamura et al. 2009; Ishihara et al. 2010). In addition to the much improved sensitivity and spatial resolution over its precursor (the *IRAS* all-sky survey), the presence of 140 and 160 μm bands is crucial to measure the peak of the dust emission at FIR wavelengths, and thus the $L_{\rm IR}$ of galaxies.

To measure $L_{\rm IR}$, we need spectroscopic redshifts of individual galaxies. We have cross-correlated the *AKARI* FIS bright source catalogue with the SDSS data release 7 (DR7) galaxy catalogue (Abazajian et al. 2009), which is the largest redshift survey in the local Universe to date.

We used a matching radius of 20 arcsec, as shown in Fig. 1. This radius is determined based mainly on the positional accuracy of

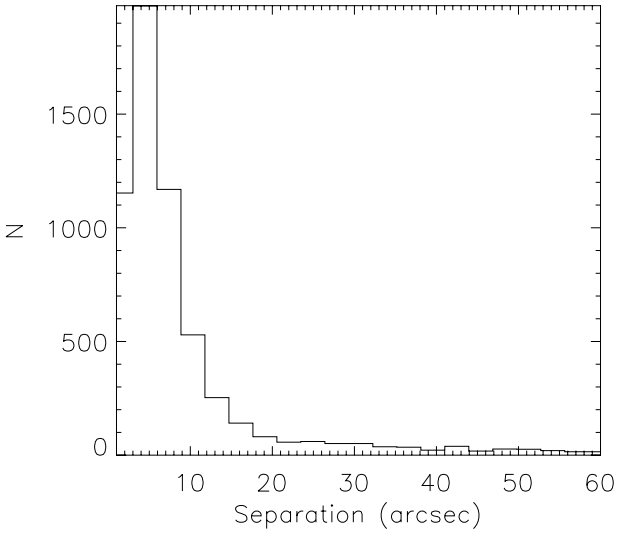

Figure 1. Angular separation between the *AKARI* Far-Infrared Surveyor (FIS) and SDSS positions. We use galaxies matched within 20 arcsec for LFs.

the *AKARI* FIR sources since for the SDSS, positional accuracy is less than 0.1 arcsec to the survey limit ($r \sim 22$; Pier et al. 2003). *AKARI*'s point spread function size in the 90 μm filter is 39 ± 1 arcsec. The astrometric accuracy of the *AKARI* FIS bright source catalogue is 3.8 arcsec in the cross-scan direction and 4.8 arcsec in the in-scan direction (Yamamura et al. 2009). The 20 arcsec radius also accounts for the physical shift that could be present between the peaks of the FIR and the optical emission. At the median redshift of $z = 0.031$, 20 arcsec corresponds to 12 kpc. The source density of the SDSS main spectroscopic galaxies is 92 deg^{-2} (Strauss et al. 2002). Therefore, within the 20 arcsec around each *AKARI* source, 0.009 background galaxies are expected to be present, i.e. less than 1 per cent of our sources are expected to be a chance coincidence, which should not affect our estimate of the LFs [see Sutherland & Saunders (1992) for a maximum likelihood approach to this].

We do not use galaxies at $z < 0.01$ since (i) at such a low velocity, uncertainty from peculiar velocity is too large to estimate distance from spectroscopic redshift, and (ii) *AKARI*'s photometry of largely extended objects is not finalized yet. We also remove galaxies at $z \geq 0.3$ to avoid too much evolutionary effect within the redshift range. We also use SDSS galaxies with extinction corrected $r_{\rm petro} \leq 17.7$, where the SDSS main galaxy spectroscopic target selection can be considered complete. To obtain reliable LFs, we only use *AKARI* sources with $S_{90\,\mu{\rm m}} > 0.7$ Jy, where completeness is greater than 80 per cent. Among these, 99 per cent of sources have a high-quality flag of FQUAL = 3 at 90 μm. 67 per cent of *AKARI* sources with $S_{90\,\mu{\rm m}} > 0.7$ Jy in the area covered by the SDSS had an optical counterpart. The rest of the sources are either stars or galaxies fainter than $r_{\rm petro} = 17.7$, which are properly accounted for in the LF computation in Section 3.1.

The previous sample of local IR LFs was based on *IRAS* $S_{60\,\mu{\rm m}}$ flux, and thus it has been a concern that colder galaxies, whose FIR emission peaks at larger wavelengths, might have been missed in the sample. Our sample is selected using $S_{90\,\mu{\rm m}}$ flux, and thus is more robust to such a selection bias.

We found cross-matches of 2357 galaxies, with which we will measure IR LFs. Among these, 97, 98 and 87 per cent of sources have measured flux at 65, 140 and 160 μm. For these sources the *AKARI* IRC catalogue is also cross-matched. Only 0.8 per cent of FIS-SDSS sources do not have an IRC counterpart within 20 arcsec. Fig. 2 shows a redshift distribution of the sample. The number of galaxies used is similar to the *IRAS*-based work by Goto (2005), despite the factor of 2 increase in the optical (SDSS) sample. This is due to the more stringent cross-matching criterion we used. *AKARI*'s improved astrometry allowed us to remove ambiguous cross-IDs. Nevertheless, thanks to the large sky coverage of the SDSS and *AKARI* surveys, this is one of the largest number of galaxies used to construct IR LFs. For example, previous local IR LFs are based on ∼600 galaxies (Sanders et al. 2003; Goto et al. 2011).

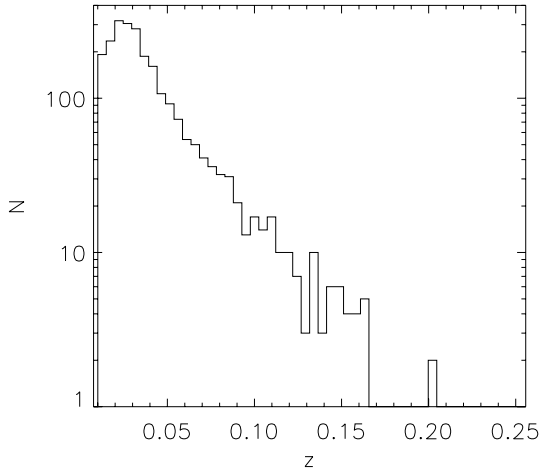

Figure 2. Redshift distribution of the *AKARI*-SDSS galaxies.

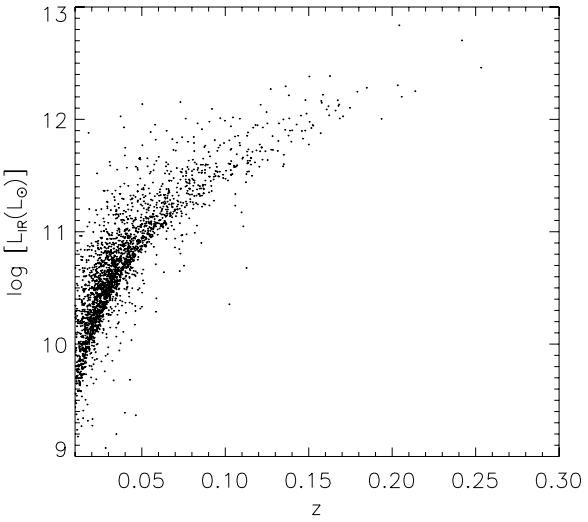

Figure 3. $L_{\rm IR}$ measured by the *AKARI* as a function of spectroscopic redshift.

2.2 Estimating total IR luminosity

For these galaxies, we estimated total IR luminosities ($L_{\rm IR}$) by fitting the *AKARI* photometry with SED templates. We used the LePhare code[1] to fit the IR part (>7 μm) of the SED. We fit our *AKARI* FIR photometry with the SED templates from Chary & Elbaz (2001, hereafter CHEL), which showed the most promising results among SED models tested by Goto et al. (2011). It is a concern that the CHEL models do not include SEDs for AGN. However, we show later in Section 2.3 that this is not a major problem using observed data. We did not include *IRAS* photometry in the SED fit partly because the better spatial resolution of *AKARI* often resolves background cirrus and nearby companions better (Jeong et al. 2007), and partly because not all of the *AKARI* sources are detected with *IRAS* due to the difference in flux limits. Although the shape of these SEDs is luminosity-dependent, the large baseline from *AKARI* observations (*S*9*W*, *L*18*W*, *N*60, *WS*, *WL* and *N*160) allows us to adopt a free scaling to obtain the best SED fit, which is then rescaled to derive $L_{\rm IR}$. To be precise, we only used ≥65 μm flux to free scale the SEDs since mid-IR bands can sometimes be affected by the stellar emission. For those sources with a low-quality flag (FQUAL = 1), we adopted a minimum error of 25 per cent. In this work, $L_{\rm IR}$ is measured in the wavelength range of 8–1000 μm. Fig. 3 shows $L_{\rm IR}$ as a function of spectroscopic redshift.

2.3 AGN/SFG separation

One has to be careful that two different physical mechanisms contribute to the total IR emission of galaxies: one by SF and the other by AGN. It is therefore fundamental to separate the IR contribution from these two different physics, to understand the evolution of the

[1] http://www.cfht.hawaii.edu/∼arnouts/lephare.html

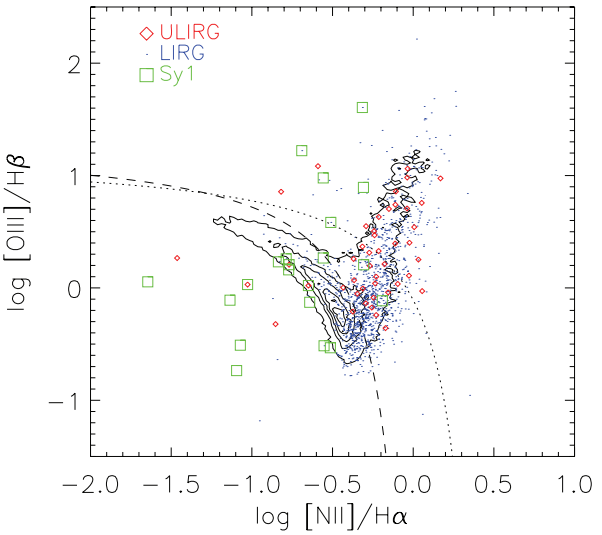

Figure 4. Emission-line ratios used to select AGNs from our sample. The contour shows the distribution of all galaxies in the SDSS with $r < 17.77$ (regardless of IR detection). The dotted line is the criterion between starbursts and AGN described in Kewley et al. (2001). The dashed line is the criterion by Kauffmann et al. (2003). Galaxies with line ratios higher than the dotted line are regarded as AGN. Galaxies below the dashed line are regarded as star-forming. Galaxies between the dashed and dotted lines are regarded as composites. The blue and red dots are for ULIRGs and LIRGs, respectively. The green squares are Seyfert 1 galaxies identified by eye-balling optical spectra.

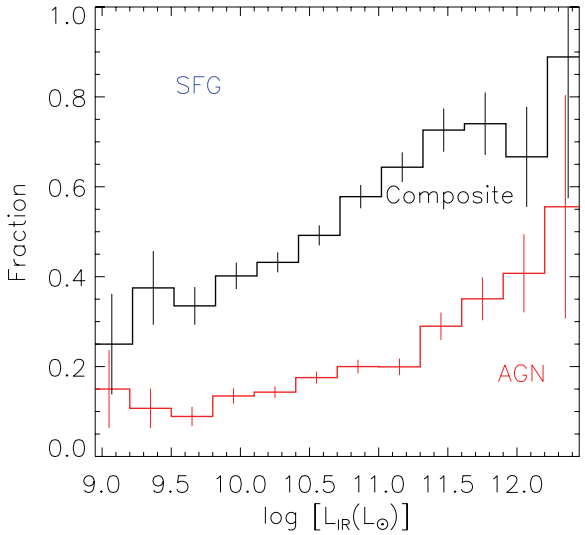

Figure 5. Fractions of AGN and composite galaxies as a function of $L_{\rm IR}$. AGN are classified using Kewley et al. (2001) among galaxies with all four lines measured. Composite galaxies include those classified as AGN using Kauffmann et al. (2003).

SF and AGN activity. However, this has been notoriously difficult and has been a subject of active debate over the last decades. Many AGN/SF separation methods have been proposed such as X-ray, radio luminosity, optical line ratios, PAH strengths, submillimetre properties and so on (Zhu et al. 2008; Sajina et al. 2008; LaMassa et al. 2010). Often, not all of the indicators agree with one another, partly due to the complicated nature of IR sources (multiple core, composite, etc).

In this work, since we have optical spectra of individual galaxies, we use [N II]/Hα versus [O III]/Hβ line ratios to classify galaxies into AGN or SFG. In Fig. 4, we plot [N II]/Hα against [O III]/Hβ line ratios. The black contours show the distribution of all emission-line galaxies in the SDSS, regardless of the *AKARI* detection. The dotted and dashed lines are the AGN/SFG separation criteria presented by Kewley et al. (2001) and Kauffmann et al. (2003), respectively. We regard galaxies above the dotted line as AGN, below the dashed line as SFG and those in between as composite galaxies.

Although these line diagnosis criteria work well for narrow-line AGN, they could be problematic for broad-line AGN. Although, in principle, one could separate narrow-line components from broad-line by multiple-line fitting, it is often difficult with weak lines on noisy spectra. To see how well broad-line AGN are classified in Fig. 4, one of us (MM) has eyeballed all emission-line IR galaxies with FWHM(Hα) greater than FWHM([O III]) by more than 150 km s^{-1}. We identified 22 broad-line AGN, which are shown in green squares in Fig. 4. As expected, the broad-line AGN are scattered everywhere in the figure and escape from the above criteria. Therefore, we manually overruled the classification of these broad-line AGN, and treated them as AGN in the rest of the paper, regardless of the line ratios in Fig. 4. In this process, we also came across 20 narrow-line AGN (although these are not a complete sample). They were successfully classified as AGN in Fig. 4.

In Fig. 4, ultraluminous infrared galaxies (ULIRGs) and luminous infrared galaxies (LIRGs) are marked with red diamonds and blue dots, respectively. It is interesting that the majority of (U)LIRGs are aligned along the AGN branch of the diagram, implying the AGN fraction is high among (U)LIRGs. This is more clearly seen in Fig. 5, where we plot fractions of AGN as a function of $L_{\rm IR}$. The red solid line shows fractions of AGN only, and the black dotted line includes composite galaxies. Note that the fractions do not include completely obscured sources in the optical for both SFG and AGN. The fractions of AGN (including composites) increase from 15 per cent (25 per cent) at log $L_{\rm IR} = 9.0$ to 55 per cent (90 per cent) at log $L_{\rm IR} = 12.3$. These results agree with previous AGN fraction estimates (Goto 2005; Yuan, Kewley & Sanders 2010; Kartaltepe et al. 2010). The improvement in this work is that due to much larger statistics, we were able to show fractions of AGN in much finer luminosity bins, more accurately quantifying the increase. In particular, a sudden increase of $f_{\rm AGN}$ at log $L_{\rm IR} > 11.3$ is notable due to the increased statistics in this work.

Having AGN/SFG classified, in Fig. 6, we show rest-frame SEDs of AGN (red triangles) and SFG (blue squares) separately. Note that only galaxies detected in all the six *AKARI* bands are shown here. The fluxes are normalized at 90 μm. The solid lines connect median points for each sample. In Fig. 6, there is no significant difference between AGN and SFG SEDs. This has two implications: although the CHEL SED models do not include SEDs for AGN, the SED fit can be performed using the galaxy SED models. At the same time, we need to be careful that although we selected AGN based on the optical line ratios, IR SEDs of these optically selected AGN can be dominated by SF activity in the AGN host galaxy.

In Fig. 7, we show the star formation rate (SFR) computed from the self-absorption and extinction-corrected Hα flux (Goto 2005) against $L_{\rm IR}$ for SFGs. The SFR is also corrected for the fibre loss of the SDSS spectrograph. There is a correlation, but compared with the well-known relation by Kennicutt (1998), there is a significant offset. This might warn us of a simple application of Kennicutt (1998)'s law to IR luminous galaxies. Kennicutt (1998)'s sample was dominated by more regular (less IR luminous) spiral galaxies, whose $L_{\rm IR}$ might stem from cool cirrus clouds warmed by older

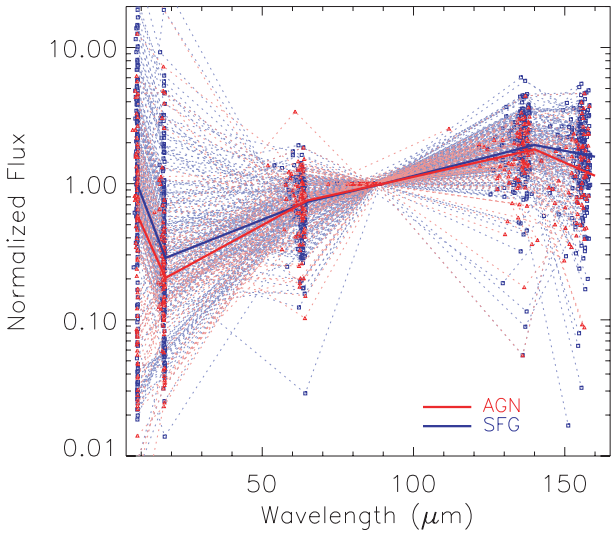

Figure 6. SEDs of AGN (red triangles) and SFG (blue squares). The red and blue solid lines connect median values for AGN and SFG, respectively. Note that only galaxies detected in all the six *AKARI* bands are shown here. The fluxes are normalized at 90 μm.

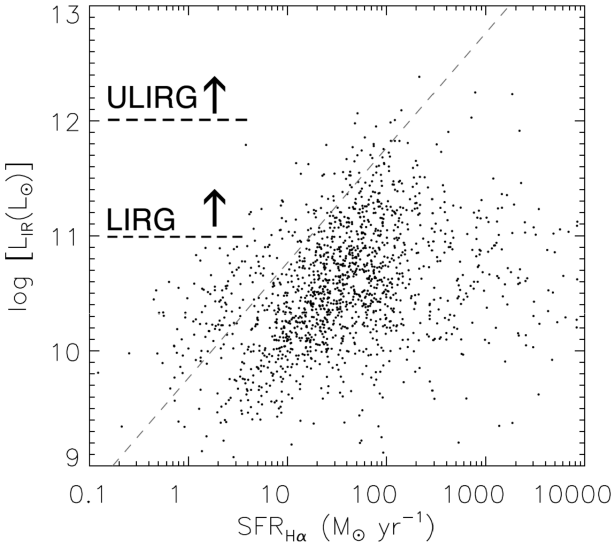

Figure 7. The SFR computed from the Hα emission line is plotted against the total IR luminosity (L_{IR}). The Hα lines are corrected for stellar absorption and extinction using the Balmer decrement. AGN are excluded from this figure using Fig. 4.

stars. This might not be the case for vigorously star-forming LIRGs and ULIRGs with hot dust.

In Fig. 8, we plot the self-absorption-corrected Hα/Hβ ratio as a function of L_{IR} for SFG. Although the median in the solid line shows a slight increase with increasing Hα/Hβ ratio, it has a large scatter, suggesting that not only L_{IR} decides the dust extinction in galaxies.

In Fig. 9, we plot L_{IR} versus $L_{[O\,III]}$. Only objects classified as AGN are shown here. Both of these luminosities are considered to be good indicators of the AGN power, and there is a recognizable correlation, however, with a significant scatter. The exact reason for the scatter is unknown but possible causes include contamination from H II regions, cirrus emission, shocks and emission from a very

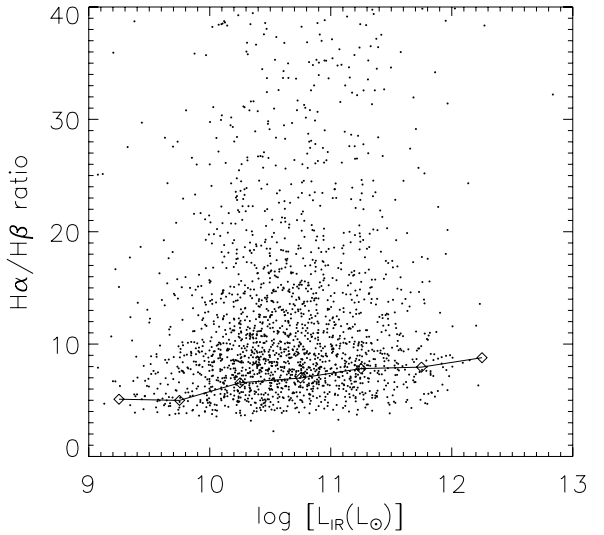

Figure 8. The self-absorption-corrected Hα/Hβ ratios are shown against L_{IR} for SFG. The solid line connects median values.

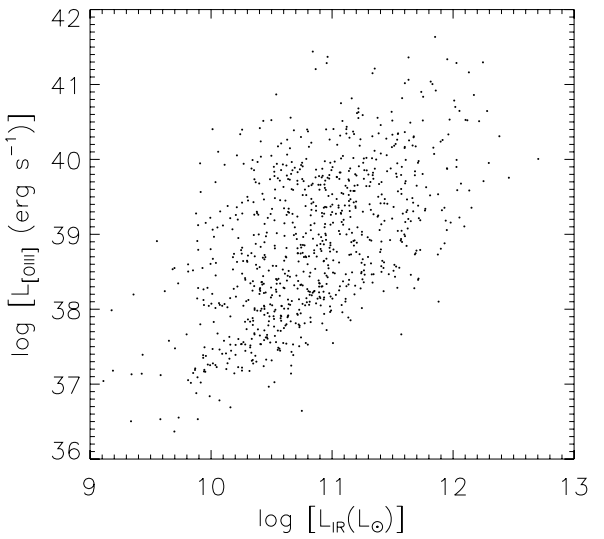

Figure 9. Luminosity of the [O III](5008 Å) emission line is plotted against total IR luminosity for AGN. Only objects classified as AGN are shown here.

small narrow-line region directly powered by an accreting black hole.

In Fig. 10, we show the rest-frame $u - r$ versus M_r colour–magnitude diagram. We used Blanton et al. (2003, v4_1) for k-correction. The contours show the distribution of all SDSS galaxies with $r < 17.7$ regardless of IR detection. ULIRGs and LIRGs do not follow either the red-sequence at $u - r \sim 2.6$ or the blue cloud at $u - r < 2.0$, but are widely distributed in $u - r$ colour. As expected, ULIRGs are more luminous in M_r than LIRGs.

The red squares, green diamonds and blue dots are for AGN, composite and SF IR galaxies classified using Fig. 4. These IR galaxies also show a wide distribution in Fig. 10, with AGN slightly brighter than the composites, reflecting the fact that the AGN fractions are higher for more luminous objects (Fig. 5). The SFG are slightly more extended to bluer clouds than AGN and the composites. These distributions are consistent with AGN and IR galaxies populating the so-called 'green valley' between the red-sequence

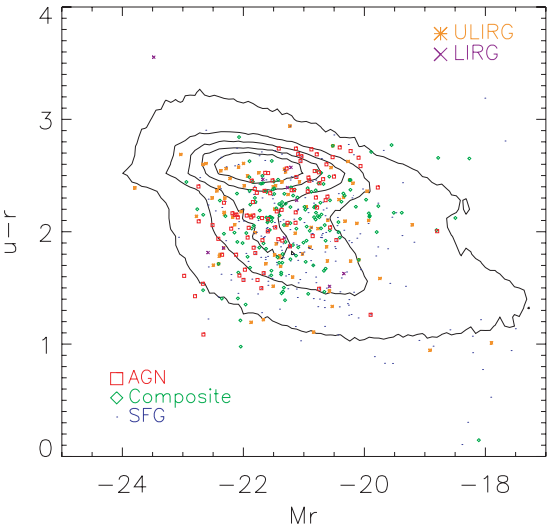

Figure 10. Rest-frame $u - r$ versus M_r colour–magnitude diagram. The contours show the distribution of all SDSS galaxies with $r < 17.7$. The orange stars and crosses denote ULIRGs and LIRGs in our sample. The red square, green diamond and blue dots are for AGN, composite and SF IR galaxies classified using Fig. 4.

and blue clouds (Smolčić 2009; Schawinski et al. 2010). Perhaps physical reasons deciding $u - r$ colour are different for AGN and SFG. For example, dust reddening might play a significant role for SFG, especially IR luminous ones. For AGN, lack of gas in red-sequence galaxies and dominance of H II regions in blue-cloud galaxies may push AGN into the green valley.

We caution readers that our AGN/SFG classification is by no means complete, but merely one attempt. In reality most galaxies have both AGN and SF, and thus contributions to $L_{\rm IR}$ and $L_{[\rm O\,III]}$ from both components. When one is dominant, it is difficult to assess a contribution from the other, which inevitably becomes a contamination to the former. Recently, it has been reported that to fit the FIR SED of AGN dominant galaxies, one always needs a starburst component, even for quasars (Shao et al. 2010; Hatziminaoglou et al. 2010; Pozzi et al. 2010). In this sense, our $L_{\rm IR}$ of AGN includes IR emission from an AGN host galaxy. The latter might be dominant at FIR wavelengths. Galaxies with line ratios consistent with being LINERs are treated as AGN in this paper, but their emission may have nothing to do with an accreting black hole, and instead may be from shocks or something else. Therefore, it is possible that these classified as AGN in this paper still have significant IR emission from host galaxies, instead of central black holes. To make the matter worse, it is unknown how many completely obscured galaxies we miss in our optical classification for both AGN and SFG. While this work had only optical line ratios for classification, the final conclusion must be based on multi-wavelength data.

3 INFRARED LUMINOSITY FUNCTIONS

3.1 The $1/V_{\rm max}$ method

With accurately measured $L_{\rm IR}$, we are ready to construct IR LFs. Since our sample is flux-limited at $r = 17.7$ and $S_{90\,\mu\rm m} = 0.7$ Jy, we need to correct for a volume effect to compute LFs. Thus, we used the $1/V_{\rm max}$ method (Schmidt 1968). An advantage of the $1/V_{\rm max}$ method is that it allows us to compute an LF directly from data, with no parameter dependence or a model assumption. A drawback is that it assumes a homogeneous galaxy distribution and thus is vulnerable to local over-/underdensities (Takeuchi, Yoshikawa & Ishii 2000).

A comoving volume associated with any source of a given luminosity is defined as $V_{\rm max} = V_{z_{\rm max}} - V_{z_{\rm min}}$, where $z_{\rm min}$ is the lower limit of the redshift and $z_{\rm max}$ is the maximum redshift at which the object could be seen given the flux limit of the survey. In this work, we set $z_{\rm min} = 0.01$ since at a very small redshift, an error in redshift measurement is dominated by a peculiar motion, and thus, $L_{\rm IR}$ also has a large error.

For the IR detection limit, we used the same SED templates (CHEL) as we used to compute $L_{\rm IR}$ for the k-correction to obtain the maximum observable redshift from the $S_{90\,\mu\rm m}$ flux limit. For the optical detection limit, we used Blanton et al. (2003, v4_1) for k-correction. We adopted a redshift where galaxies become fainter than either r- or the $S_{90\,\mu\rm m}$-flux limit as $z_{\rm max}$.

For each luminosity bin then, the LF is derived as

$$\phi = \frac{1}{\Delta L} \sum_i \frac{1}{V_{{\rm max},i}} w_i, \qquad (1)$$

where $V_{\rm max}$ is a comoving volume over which the ith galaxy could be observed, ΔL is the size of the luminosity bin and w_i is the completeness correction factor of the ith galaxy. Note that the $V_{\rm max}$ method considers both the optical and IR flux limits. Therefore, even in an IR source with $r > 17.7$, a detectable volume of such sources is properly considered by the $V_{\rm max}$ method as long as IR sources with the same optical-to-IR ratio can be detected at a lower redshift [see appendix of Serjeant et al. (2001) and Avni & Bahcall (1980) for more details of a multi-variate $V_{\rm max}$ method]. A very obscured IR galaxy (with $r > 17.7$ even at the lowest redshift of $z = 0.01$), however, would have a detectable volume of zero, and thus would not be included in the LF computation. The number density of such obscured IR galaxies is a matter of interest itself, but requires deeper optical data. Although we cannot test a deeper r-band criterion since the SDSS spectroscopic survey stops at the current limit, we can test a brighter r-band criterion. We computed the LF using a brighter r-band criterion by 1 mag, at $r < 16.7$. The resulting LF was noisier due to the reduced number of galaxies used, but essentially the same as the LF presented in the following sections. The test suggests that the $V_{\rm max}$ method works well. We used the completeness correction measured in the FIS bright source catalogue release note for $S_{90\,\mu\rm m}$ flux. This correction is 25 per cent at maximum, since we only use the sample where the completeness is greater than 80 per cent. The completeness correction in terms of sky coverage of both surveys is taken into account.

3.2 Monte Carlo simulation

Uncertainties in the LF values stem from various factors such as the finite numbers of sources in each luminosity bin, the k-correction uncertainties and the flux errors. To compute these errors we performed Monte Carlo simulations by creating 150 simulated catalogues, where each catalogue contains the same number of sources, but we assign to each source new fluxes following a Gaussian distribution centred at fluxes with a width of a measured error. Then, we measured errors of each bin of the LF based on the variation in the 150 simulations. These estimated errors are added in quadrature to the Poisson errors in each LF bin.

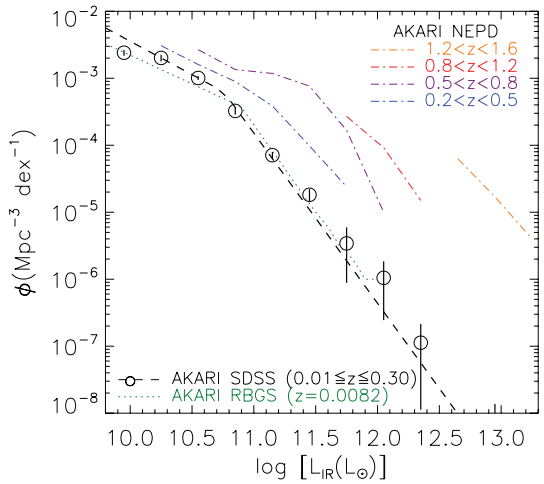

Figure 11. IR LF of *AKARI*-SDSS galaxies. The $L_{\rm IR}$ is measured using the *AKARI* 9, 18, 65, 90, 140 and 160 μm fluxes through an SED fit. Errors are computed using 150 Monte Carlo simulations, added by the Poisson error. The dotted lines show the best-fitting double power law. The green dotted lines show IR LF at $z = 0.0082$ by Goto et al. (2011). The dash–dotted lines are higher redshift results from the *AKARI* NEP deep field (Goto et al. 2010a).

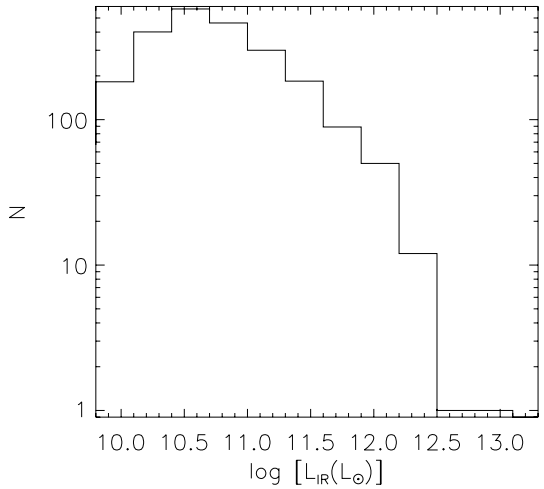

Figure 12. An IR luminosity histogram of galaxies used to compute Fig. 11.

3.3 IR luminosity function

In Fig. 11, we show IR LF of the *AKARI*-SDSS galaxies, followed by Fig. 12, which shows the number of galaxies used to compute the LF. The median redshift of our sample galaxies is $z = 0.031$. Overplotted in green dotted lines is the IR LF of Revised Bright Galaxy Sample (RBGS) at $z = 0.0082$ but with re-measured $L_{\rm IR}$ based on the *AKARI* six-band photometry (Goto et al. 2011). Our LF agrees very well with that from the RBGS (Sanders et al. 2003; Goto et al. 2011). Although it was a concern that the RBGS was $S_{60\,\mu\rm m}$ selected, the agreement suggests that the selection does not affect the total IR LF, perhaps because 60 μm is close to the peak of the dust emission and captures most IR galaxies. Dotted lines show higher redshift results from the *AKARI* NEP deep field (Goto et al. 2010a). Our results (open circles) agree with that from $z = 0.0082$, and show smooth evolution towards higher redshift. The faint-end slope of our sample agrees well with immediately higher/lower redshift LFs.

Table 1. Best double power-law fit parameters for the *AKARI* LFs.

Sample	$L^*_{\rm IR}$ ($\rm L_\odot$)	ϕ^*($\rm Mpc^{-3}\,dex^{-1}$)	α (faint-end)	β (bright-end)
Total	$5.7 \pm 0.2 \times 10^{10}$	0.00062 ± 0.00002	1.99 ± 0.09	3.54 ± 0.09
SFG	$5.0 \pm 0.2 \times 10^{10}$	0.00043 ± 0.00003	1.8 ± 0.1	3.5 ± 0.3
AGN	$4.3 \pm 0.2 \times 10^{10}$	0.0004 ± 0.0001	1.4 ± 0.1	3.1 ± 0.2

Following Sanders et al. (2003), we fit an analytical function to the LFs. In the literature, IR LFs were fitted better by a double power law (Babbedge et al. 2006; Goto et al. 2010a,c) or a double exponential (Pozzi et al. 2004; Le Floc'h et al. 2005; Takeuchi et al. 2006) than a Schechter function, which steeply declines at the high luminosity and underestimates the number of bright galaxies. In this work, we fit the IR LFs using a double power law (Babbedge et al. 2006) as follows:

$$\Phi(L)\,{\rm d}L/L^* = \Phi^* \left(\frac{L}{L^*}\right)^{1-\alpha} {\rm d}L/L^*, \quad (L < L^*) \tag{2}$$

$$\Phi(L)\,{\rm d}L/L^* = \Phi^* \left(\frac{L}{L^*}\right)^{1-\beta} {\rm d}L/L^*, \quad (L > L^*). \tag{3}$$

Free parameters are L^* (characteristic luminosity, $\rm L_\odot$), ϕ^* (normalization, $\rm Mpc^{-3}$), α and β (faint- and bright-end slopes), respectively. The best-fitting values are summarized in Table 1. In Fig. 11, the dashed line shows the best-fitting double power law. The local LF has a break at $L^* = 5.7 \pm 0.2 \times 10^{10}\,\rm L_\odot$. Understanding how this break (L^*) evolves as a function of cosmic time, and what causes the break, is fundamental to galaxy evolution studies. This work provides an important benchmark in the local Universe.

3.4 Bolometric IR luminosity density based on the IR LF

One of the primary purposes in computing IR LFs is to estimate the IR luminosity density, which in turn is a good estimator of the dust-hidden cosmic SF density (Kennicutt 1998), once the AGN contribution is removed. The bolometric IR luminosity of a galaxy is produced by thermal emission of its interstellar matter. In SF galaxies, the UV radiation produced by young stars heats the interstellar dust, and the reprocessed light is emitted in the IR. For this reason, in SFG, the bolometric IR luminosity is a good estimator of the current SFR of the galaxy.

Once we have measured the LF, we can estimate the total IR luminosity density by integrating the LF, weighted by the luminosity. We used the best-fitting double power law to integrate outside the luminosity range in which we have data to obtain estimates of the total IR luminosity density, $\Omega_{\rm IR}$. Note that outside of the luminosity range we have data ($L_{\rm IR} > 10^{12.5}\,\rm L_\odot$ or $L_{\rm IR} < 10^{9.8}\,\rm L_\odot$); the LFs are merely an extrapolation and thus uncertain.

The resulting total luminosity density is $\Omega_{\rm IR} = (3.8^{+5.8}_{-1.2}) \times 10^8\ \rm L_\odot\,Mpc^{-3}$. Errors are estimated by varying the fit within 1σ of uncertainty in LFs. Out of $\Omega_{\rm IR}$, 1.1 ± 0.1 per cent is produced by LIRGs ($L_{\rm IR} > 10^{11}\,\rm L_\odot$), and only 0.03 ± 0.01 per cent is by ULIRGs ($L_{\rm IR} > 10^{12}\,\rm L_\odot$). Although these fractions are larger than $z = 0.0081$, still a small fraction of $\Omega_{\rm IR}$ is produced by luminous IR galaxies at $z = 0.031$, in contrast with the high-redshift Universe. We will discuss the evolution of $\Omega_{\rm IR}$ in Section 4.1.

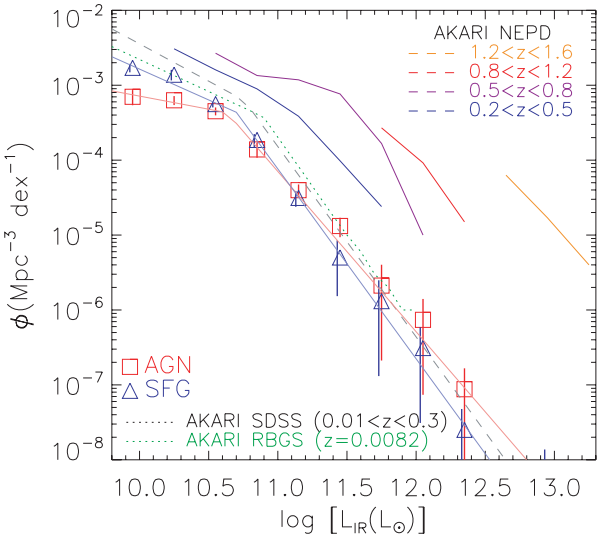

Figure 13. IR LF is separated for SFG (blue triangles) and AGN (red squares), using the classification in Fig. 4. The total IR LF in Fig. 11 is shown with the black dotted lines.

3.5 AGN/SFG IR LF

Once we have separated individual galaxies into AGN/SFG, we can construct LFs of each sample. However, we caution again that our $L_{\rm IR}$ of AGN is total IR emission of optically selected AGN, and thus it includes IR emission from AGN host galaxies. In Fig. 13, we show LFs separately for AGN (red squares) and SFG (blue triangles). Composite galaxies are included in the AGN LF. The total IR LF shown in Fig. 11 is also shown for comparison as the grey dashed line. It is interesting that both AGN and SFG IR LFs have a break at around $\log L_{\rm IR} \sim 11.0$. Then, the IR luminosity density of AGN exceeds that of SFG at $\log L_{\rm IR} > 11.0$, with flatter slope towards the brighter end. In contrast, the faint-end slope is steeper for SFG.

Next, we fit the double power law (equations 2 and 3) to the AGN and SF IR LFs, exactly as we did for the total IR LF in Fig. 11. The best-fitting parameters are summarized in Table 1. As we mentioned above, the most notable difference is at the bright- and faint-end slopes, where the AGN and SFG LFs dominate, respectively. The L^* of SFG is slightly brighter than that of AGN.

One of the pioneers in IR AGN LFs is Rush et al. (1993), who selected 893 IR galaxies (of which 118 are AGN) from *IRAS* 12 μm to minimize wavelength-dependent selection biases towards bluer Seyfert 1 nuclei and redder embedded AGN (Spinoglio & Malkan 1989). Despite small differences such as selection, AGN classification and $L_{\rm IR}$ based on *IRAS*, their total IR LF of AGN in their fig. 9 is in very good agreement with ours, showing the same AGN dominance at larger $L_{\rm IR}$.

What do these differences in LFs bring to the IR luminosity density, $\Omega_{\rm IR}$, by AGN and SFG? We estimate the total IR luminosity density by integrating the LFs weighted by the luminosity, separately for AGN and SFG. We used the double power law outside the luminosity range in which we have data to obtain estimates of the total IR luminosity density, $\Omega_{\rm IR}$, for AGN and SFG.

The resulting total luminosity density ($\Omega_{\rm IR}$) is $\Omega_{\rm IR}^{\rm SFG} = 5.9^{+1.4}_{-1.3} \times 10^7\,{\rm L}_\odot\,{\rm Mpc}^{-3}$ and $\Omega_{\rm IR}^{\rm AGN} = 1.9^{+0.5}_{-0.7} \times 10^7\,{\rm L}_\odot\,{\rm Mpc}^{-3}$, as summarized in Table 2. Errors are estimated by varying the fit within 1σ of uncertainty in LFs. The results show that among the total IR luminosity density integrated over all the IR luminosity range, 75 per cent $\Omega_{\rm IR}^{\rm SFG}/(\Omega_{\rm IR}^{\rm AGN} + \Omega_{\rm IR}^{\rm SFG})$ of IR luminosity density is emitted by the SFG, and only 24 per cent $\Omega_{\rm IR}^{\rm AGN}/(\Omega_{\rm IR}^{\rm AGN} + \Omega_{\rm IR}^{\rm SFG})$ is by AGN at $z = 0.031$. The AGN contribution is larger than $z = 0.0081$; however, it is still small compared with higher redshift results (Pérez-González et al. 2005; Le Floc'h et al. 2005; Magnelli et al. 2009; Goto et al. 2010a).

Table 2. Local IR luminosity densities by all galaxies, ULIRGs and LIRGs.

Sample	$\Omega_{\rm IR}^{\rm Total}$ (${\rm L}_\odot\,{\rm Mpc}^{-3}$)	$\Omega_{\rm IR}^{\rm LIRG}$ (${\rm L}_\odot\,{\rm Mpc}^{-3}$)	$\Omega_{\rm IR}^{\rm ULIRG}$ (${\rm L}_\odot\,{\rm Mpc}^{-3}$)
Total	$3.8^{+5.8}_{-1.2} \times 10^8$	$4.2^{+0.7}_{-0.8} \times 10^6$	$1.2^{+0.5}_{-0.4} \times 10^5$
SFG	$5.9^{+1.4}_{-1.3} \times 10^7$	$2.1^{+0.7}_{-0.8} \times 10^6$	$1.4^{+0.2}_{-0.2} \times 10^5$
AGN	$1.9^{+0.5}_{-0.7} \times 10^7$	$1.9^{+0.5}_{-0.5} \times 10^6$	$2.5^{+1.3}_{-0.9} \times 10^5$

Once we have $\Omega_{\rm IR}^{\rm SFG}$, we can estimate SF density emitted in IR light. The SFR and $L_{\rm IR}$ are related by the following equation for a Salpeter IMF, $\phi(m) \propto m^{-2.35}$ between 0.1 and 100 ${\rm M}_\odot$ (Kennicutt 1998):

$$\mathrm{SFR}[{\rm M}_\odot\,{\rm yr}^{-1}] = 1.72 \times 10^{-10} L_{\rm IR}[{\rm L}_\odot]. \quad (4)$$

By using this equation, we obtain SFR density $= (1.3 \pm 0.2) \times 10^{-2}\,{\rm M}_\odot\,{\rm yr}^{-1}$.

If we limit our integration to the ULIRG luminosity range ($L_{\rm IR} > 10^{12}\,{\rm L}_\odot$), we obtain $\Omega_{\rm IR}^{\rm SFG}({\rm ULIRG}) = 1.4^{+0.2}_{-0.2} \times 10^5\,{\rm L}_\odot\,{\rm Mpc}^{-3}$ and $\Omega_{\rm IR}^{\rm AGN}({\rm ULIRG}) = 2.5^{+1.3}_{-0.9} \times 10^5\,{\rm L}_\odot\,{\rm Mpc}^{-3}$. In other words, in the ULIRG luminosity range, AGN explain 64 per cent $\Omega_{\rm IR}^{\rm AGN}({\rm ULIRG})/[\Omega_{\rm IR}^{\rm AGN}({\rm ULIRG}) + \Omega_{\rm IR}^{\rm SFG}({\rm ULIRG})]$ of IR luminosity, again showing the AGN dominance at the bright end.

Note that $\Omega_{\rm IR}^{\rm AGN}({\rm ULIRG})$ larger than $\Omega_{\rm IR}^{\rm Total}({\rm ULIRG})$ is apparently inconsistent. This is due to the limitation in extrapolating the double power law to obtain $\Omega_{\rm IR}$. For example, the AGN LF has a flatter bright-end slope of $\beta = 3.1 \pm 0.2$ than β of 3.54 ± 0.09 for total LF. Once extrapolated to larger luminosity at $\log L_{\rm IR} > 12.5$, the flatter slope could produce larger $\Omega_{\rm IR}$ once integrated even if all the observed data points for AGN are below those of total IR. To obtain a more accurate estimate of $\Omega_{\rm IR}$ we clearly need data points in a larger luminosity range than *AKARI* observed. In this paper, we tried to obtain best estimates of each $\Omega_{\rm IR}$ for AGN, SFG and total. As a result, we caution readers that $\Omega_{\rm IR}^{\rm Total}$ is not necessarily the algebraic sum of $\Omega_{\rm IR}^{\rm AGN}$ and $\Omega_{\rm IR}^{\rm SFG}$.

In the LIRG luminosity ($L_{\rm IR} > 10^{11}\,{\rm L}_\odot$), results are $\Omega_{\rm IR}^{\rm SFG}({\rm LIRG}) = 2.1^{+0.7}_{-0.8} \times 10^6\,{\rm L}_\odot\,{\rm Mpc}^{-3}$ and $\Omega_{\rm IR}^{\rm AGN}({\rm LIRG}) = 1.9^{+0.5}_{-0.5} \times 10^6\,{\rm L}_\odot\,{\rm Mpc}^{-3}$. This shows that the AGN contribution is already down to 47 per cent $\Omega_{\rm IR}^{\rm AGN}({\rm LIRG})/[\Omega_{\rm IR}^{\rm AGN}({\rm ULIRG}) + \Omega_{\rm IR}^{\rm SFG}({\rm LIRG})]$ of IR luminosity in the LIRG range.

4 INFRARED LUMINOSITY DENSITY AND ITS EVOLUTION

4.1 Evolution of $\Omega_{\rm IR}^{\rm SFG}$

We have separated the $\Omega_{\rm IR}^{\rm SFG}$ from $\Omega_{\rm IR}^{\rm AGN}$. Now we are ready to examine the evolution of $\Omega_{\rm SFR}$ without the contribution from AGN. In Fig. 14, we plot the evolution of $\Omega_{\rm IR}^{\rm SFR}$ as a function of redshift. Higher redshift results are taken from Goto et al. (2010a), who also tried to exclude AGN using SED fitting. Results from the *Spitzer* and *GALEX* surveys are also plotted. The $\Omega_{\rm IR}^{\rm SFG}$ shows a strong evolution as a function of redshift. The best-fitting linear relation is

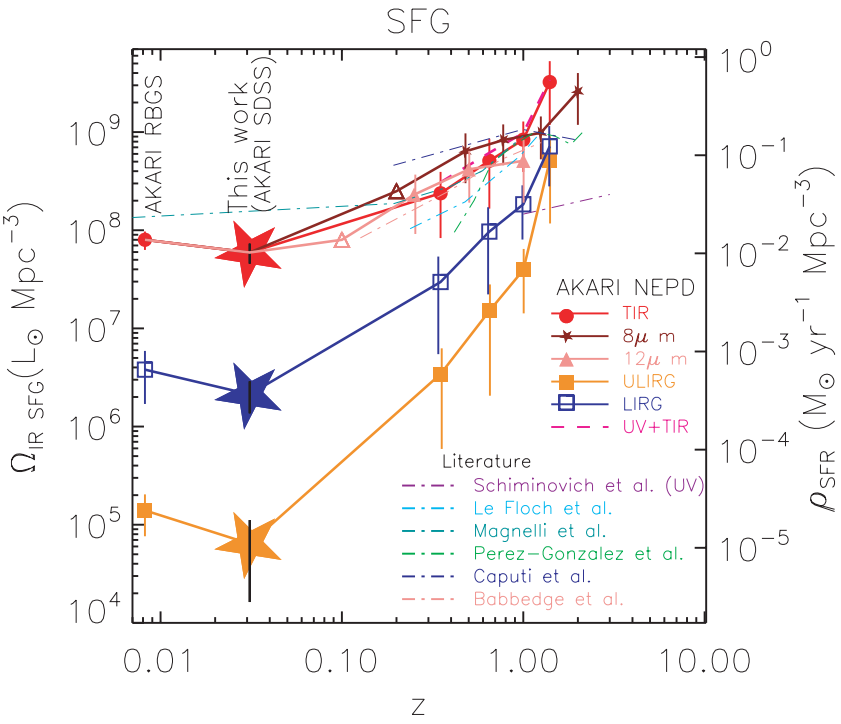

Figure 14. Evolution of IR luminosity density by SFG. Results from this work are plotted with stars at $z = 0.031$. The red, blue and orange stars show IR luminosity density from all galaxies, from LIRGs only and from ULIRGs only. Higher-redshift results in the solid lines are from the *AKARI* NEP deep field (Goto et al. 2010a). Results at $z = 0.0082$ are from the *AKARI* RBGS (Goto et al. 2011). Shown with different colours are IR luminosity density based on IR LFs (red circles), 8 μm LFs (stars) and 12 μm LFs (filled triangles). The blue open squares and orange filled squares are for only LIRGs and ULIRGs, also based on our L_{IR} LFs. Overplotted dot–dashed lines are estimates from the literature: Le Floc'h et al. (2005), Magnelli et al. (2009), Pérez-González et al. (2005), Caputi et al. (2007) and Babbedge et al. (2006) are in cyan, yellow, green, navy and pink, respectively. The purple dash–dotted line shows the UV estimate by Schiminovich et al. (2005). The pink dashed line shows the total estimate of IR (IR LF) and UV (Schiminovich et al. 2005).

$\Omega_{IR}^{SFG} \propto (1+z)^{4.1\pm0.4}$. We have removed L_{IR} of optically classified AGN in this analysis. A caveat in this process, however, is that L_{IR} of optically selected AGN perhaps includes some IR emission from SF in AGN host galaxies. In this sense, Ω_{IR}^{SFG} estimated here is a lower limit. However, this should not affect Ω_{IR}^{SFG} by more than 30 per cent since the Ω_{IR}^{AGN} is smaller than Ω_{IR}^{SFG} by a factor of 3 as we show in the next section.

In comparison, our results are in good agreement with previous works shown by the dash–dotted lines in Fig. 14. In the form of $\Omega_{IR} \propto (1+z)^{\gamma}$, Le Floc'h et al. (2005) obtained $\gamma = 3.9 \pm 0.4$, Pérez-González et al. (2005) obtained $\gamma = 4.0 \pm 0.2$, Babbedge et al. (2006) obtained $\gamma = 4.5^{+0.7}_{-0.6}$ and Magnelli et al. (2009) obtained $\gamma = 3.6 \pm 0.4$.

Once the IR luminosity density is separated into ULIRG and LIRG contributions, we found $\Omega_{IR}^{SFG}(\mathrm{ULIRG}) \propto (1+z)^{10.0\pm0.5}$ and $\Omega_{IR}^{SFG}(\mathrm{LIRG}) \propto (1+z)^{6.5\pm0.5}$. $\Omega_{IR}^{SFG}(\mathrm{ULIRG})$ shows more rapid evolution than $\Omega_{IR}^{SFG}(\mathrm{LIRG})$, showing the importance of luminous IR sources at high redshift.

4.2 Evolution of Ω_{IR}^{AGN}

In turn, we can also investigate Ω_{IR}^{AGN}. By integrating the IR $\mathrm{LF_{AGN}}$ in Fig. 13, we obtained $\Omega_{IR}^{AGN} = (1.9^{+0.5}_{-0.7}) \times 10^7\ \mathrm{L_\odot\ Mpc^{-3}}$.

In Fig. 15, we show the evolution of Ω_{IR}^{AGN}, which shows a strong evolution with increasing redshift. At a first glance, both Ω_{IR}^{AGN} and Ω_{IR}^{SFG} show rapid evolution, suggesting that the correlation between SF and black hole accretion rate continues to hold at higher redshifts, i.e. galaxies and black holes seem to be evolving hand in hand. When we fitted the evolution with $(1+z)^{\gamma}$, we found $\Omega_{IR}^{AGN} \propto (1+z)^{4.1\pm0.5}$. A caveat, however, is that Ω_{IR}^{AGN} estimated in this work is likely to include IR emission from host galaxies of AGN, although in the optical the AGN component dominates. Therefore, the final conclusion must be drawn from a multi-component fit based on better sampling in the FIR by *Herschel* or *SPICA*, to separate the AGN/SFG contribution to L_{IR}. The contribution by ULIRGs quickly increases towards higher redshift. By $z = 1.5$, it exceeds that from LIRGs. Indeed, we found $\Omega_{IR}^{AGN}(\mathrm{ULIRG}) \propto (1+z)^{8.7\pm0.6}$ and $\Omega_{IR}^{AGN}(\mathrm{LIRG}) \propto (1+z)^{5.4\pm0.5}$.

5 SUMMARY

We have cross-correlated the *AKARI* IR all-sky survey with the SDSS to find 2357 IR galaxies with optical spectra. Using *AKARI*'s six-band IR photometry at 9, 18, 65, 90, 140 and 160 μm, we have measured L_{IR} via SED model fitting. *AKARI*'s six bands cover the crucial FIR wavelengths across the peak of the dust emission, providing us with more accurate L_{IR} measurements than *IRAS*. By separating SFG/AGN using optical line ratios, we constructed local IR LFs separately for SFG and AGN. We also computed local IR luminosity density through the derived LFs, and compared Ω_{IR}^{SFG} and Ω_{IR}^{AGN} to those at higher redshifts.

Our findings are as follows.

(i) The local IR LF with the *AKARI* data at the median redshift of $z = 0.031$ agrees well with that at $z = 0.0081$, and shows smooth and continuous evolution towards higher redshift results from the *AKARI* NEP deep field.

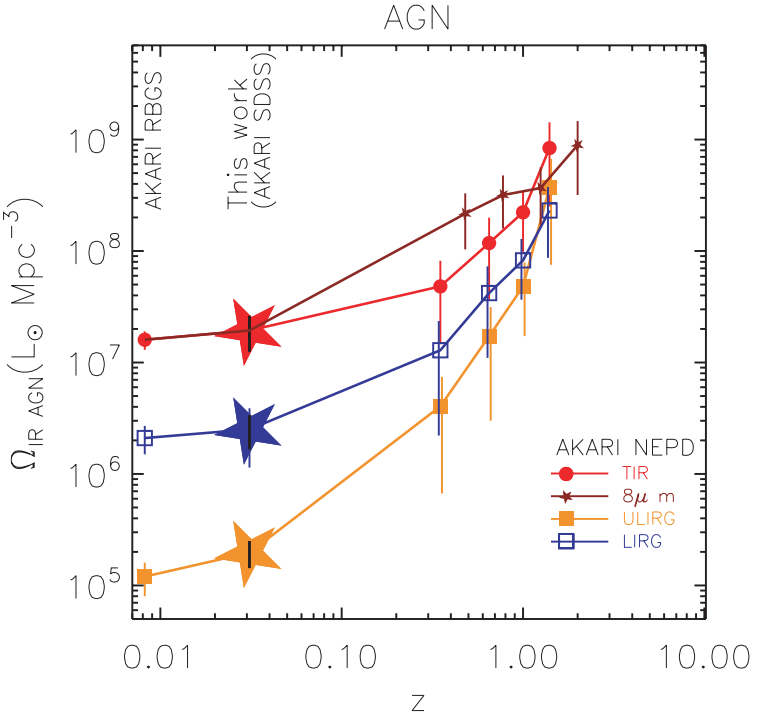

Figure 15. Evolution of IR luminosity density by AGN. Results from this work are plotted with stars at the median redshift of $z = 0.031$. The red, blue and orange points show IR luminosity density from all AGN, from LIRG AGN only and from ULIRG AGN only. Higher redshift results are from the *AKARI* NEP deep field (Goto et al. 2010a), with contributions from SFG removed. Brown triangles are Ω_{IR}^{AGN} computed from the 8 μm LFs (Goto et al. 2010a). Results at $z = 0.0082$ are from the *AKARI* RBGS (Goto et al. 2011).

(ii) By integrating the IR LF weighted by L_{IR}, we obtain the local cosmic IR luminosity density of $\Omega_{IR} = (3.8^{+5.8}_{-1.2}) \times 10^8\,L_\odot\,Mpc^{-3}$.

(iii) The fraction of AGN and composite galaxies shows a continuous increase from 25 to 90 per cent at $9 < \log L_{IR} < 12.5$.

(iv) The SFR based on self-absorption, and extinction-corrected Hα, correlates with L_{IR} for SFGs.

(v) The Hα/Hβ ratio shows a weak increase with L_{IR}, however with a large scatter.

(vi) $L_{[O\,III]}$ correlates well with L_{IR} for AGN.

(vii) The AGN contribution to Ω_{IR} becomes dominant at $L_{IR} > 10^{11}\,L_\odot$, above the break of the both SFG and AGN IR LFs. At $L_{IR} \leq 10^{11}\,L_\odot$, SFG dominates IR LFs.

(viii) LIRGs and ULIRGs contribute to Ω_{IR} a little. Only 1.1 ± 0.1 per cent of Ω_{IR} is produced by LIRGs ($L_{IR} > 10^{11}\,L_\odot$), and only 0.03 ± 0.01 per cent by ULIRGs ($L_{IR} > 10^{12}\,L_\odot$) in the local Universe.

(ix) Compared with high-redshift results from the *AKARI* NEP deep survey, we observed a strong evolution of $\Omega_{IR}^{SFG} \propto (1+z)^{4.1\pm0.4}$ and $\Omega_{IR}^{AGN} \propto (1+z)^{4.1\pm0.5}$.

ACKNOWLEDGMENTS

We thank the anonymous referee for many insightful comments, which significantly improved the paper.

TG acknowledges financial support from the Japan Society for the Promotion of Science (JSPS) through JSPS Research Fellowships for Young Scientists.

This research is based on observations with *AKARI*, a JAXA project with the participation of ESA.

The authors wish to recognize and acknowledge the very significant cultural role and reverence that the summit of Mauna Kea has always had within the indigenous Hawaiian community. We are most fortunate to have the opportunity to conduct observations from this sacred mountain.

TTT has been supported by the Program for Improvement of Research Environment for Young Researchers from Special Coordination Funds for Promoting Science and Technology, and the Grant-in-Aid for the Scientific Research Fund (20740105) commissioned by the Ministry of Education, Culture, Sports, Science and Technology (MEXT) of Japan. TTT has been also partially supported from the Grand-in-Aid for the Global COE Program 'Quest for Fundamental Principles in the Universe: from Particles to the Solar System and the Cosmos' from the MEXT.

REFERENCES

Abazajian K. N. et al., 2009, ApJS, 182, 543
Avni Y., Bahcall J. N., 1980, ApJ, 235, 694
Babbedge T. S. R. et al., 2006, MNRAS, 370, 1159
Blanton M. R. et al., 2003, AJ, 125, 2348
Caputi K. I. et al., 2007, ApJ, 660, 97
Chary R., Elbaz D., 2001, ApJ, 556, 562 (CHEL)
Dunne L., Eales S. A., 2001, MNRAS, 327, 697
Goto T., 2005, MNRAS, 360, 322
Goto T. et al., 2010a, A&A, 514, A6
Goto T. et al., 2010b, A&A, 514, A7
Goto T. et al., 2011, MNRAS, 410, 573
Gruppioni C. et al., 2010, A&A, 518, L27
Hatziminaoglou E. et al., 2010, A&A, 518, L33
Ishihara D. et al., 2010, A&A (*AKARI* Special Issue), in press
Jeong W.-S. et al., 2007, PASJ, 59, 429
Kartaltepe J. S. et al., 2010, ApJ, 709, 572
Kauffmann G. et al., 2003, MNRAS, 346, 1055
Kennicutt R. C., Jr, 1998, ARA&A, 36, 189
Kewley L. J., Dopita M. A., Sutherland R. S., Heisler C. A., Trevena J., 2001, ApJ, 556, 121

LaMassa S. M., Heckman T. M., Ptak A., Martins L., Wild V., Sonnentrucker P., 2010, ApJ, 720, 786
Le Floc'h E. et al., 2005, ApJ, 632, 169
Magnelli B., Elbaz D., Chary R. R., Dickinson M., Le Borgne D., Frayer D. T., Willmer C. N. A., 2009, A&A, 496, 57
Murakami H. et al., 2007, PASJ, 59, 369
Pérault M., 1987, PhD thesis
Pérez-González P. G. et al., 2005, ApJ, 630, 82
Pier J. R., Munn J. A., Hindsley R. B., Hennessy G. S., Kent S. M., Lupton R. H., Ivezić Ž., 2003, AJ, 125, 1559
Pozzi F. et al., 2004, ApJ, 609, 122
Pozzi F. et al., 2010, A&A, 517, A11
Rodighiero G. et al., 2010, A&A, 515, A8
Rush B., Malkan, M., Spinoglio L., 1993, ApJS, 89, 1
Sajina A. et al., 2008, ApJ, 683, 659
Sanders D. B., Mazzarella J. M., Kim D.-C., Surace J. A., Soifer B. T., 2003, AJ, 126, 1607
Schawinski K. et al., 2010, ApJ, 711, 284
Schiminovich D. et al., 2005, ApJ, 619, L47
Schmidt M., 1968, ApJ, 151, 393
Serjeant S. et al., 2001, MNRAS, 322, 262
Shao L. et al., 2010, A&A, 518, L26
Smolčić V., 2009, ApJ, 699, L43
Spinoglio L., Malkan M. A., 1989, ApJ, 342, 83
Strauss M. A. et al., 2002, AJ, 124, 1810
Sutherland W., Saunders W., 1992, MNRAS, 259, 413
Symeonidis M., Page M. J., Seymour N., Dwelly T., Coppin K., McHardy I., Rieke G. H., Huynh M., 2009, MNRAS, 397, 1728
Takeuchi T. T., Yoshikawa K., Ishii T. T., 2000, ApJS, 129, 1
Takeuchi T. T., Ishii T. T., Dole H., Dennefeld M., Lagache G., Puget J.-L., 2006, A&A, 448, 525
Treister E., Urry C. M., Virani S., 2009, ApJ, 696, 110
Yamamura I. et al., 2009, AIP Conf. Ser. Vol. 1158, Exoplanets and disks: their formation and diversity. Am. Inst. Phys., New York, p. 169
Yuan T.-T., Kewley L. J., Sanders D. B., 2010, ApJ, 709, 884
Zhu Y.-N., Wu H., Cao C., Li H.-N., 2008, ApJ, 686, 155

This paper has been typeset from a TEX/LATEX file prepared by the author.